

## Strong Polarization Transformation of Bloch Surface Waves

Junxue Chen,<sup>1</sup> Douguo Zhang,<sup>2,\*</sup> Pei Wang,<sup>2</sup> Hai Ming,<sup>2</sup> and Joseph R. Lakowicz<sup>3</sup>

<sup>1</sup>School of Science, Southwest University of Science and Technology, Mianyang, Sichuan 621010, China

<sup>2</sup>Institute of Photonics, Department of Optics and Optical Engineering,

University of Science and Technology of China, Hefei, Anhui 230026, China

<sup>3</sup>Center for Fluorescence Spectroscopy, Department of Biochemistry and Molecular Biology,

University of Maryland School of Medicine, Baltimore, Maryland 21201, USA



(Received 27 October 2017; revised manuscript received 16 December 2017; published 9 February 2018)

Polarization is an intrinsic attribute of optical waves, so manipulating the polarization state of optical surface waves can be of fundamental importance for next-generation information and biophotonics technology. Here, we show theoretically that the polarization of the Bloch surface wave (BSW) on a dielectric multilayer can be transformed between a transverse-electric state and a transverse-magnetic state by using the laterally continuous grooves inscribed on this multilayer. This polarization transformation can be enhanced or inhibited by the interference between the reflected BSW beams, which can be tuned by the periodicity and depth of the grooves. Maximum polarization transformation efficiency can be achieved as high as 43% when the number of grooves is increased to ten. A generalized Fresnel formula is proposed to describe the polarization transformation of the BSW beams. Because of this polarization transformation, an anomalous reflection of BSW beams can be realized, which is the inequality between the incident angle and the reflection angle.

DOI: [10.1103/PhysRevApplied.9.024008](https://doi.org/10.1103/PhysRevApplied.9.024008)

### I. INTRODUCTION

Bloch surface waves (BSWs), the electromagnetic surface waves excited at the interface between a truncated periodic dielectric multilayer with a photonic band gap and its surrounding medium have been considered as the dielectric analogue of surface-plasmon polaritons (SPPs) that are also the electromagnetic surface waves but propagate at the interface between a metallic film and its dielectric cladding [1,2]. Similar to the SPPs, BSWs can also induce the optical near-field confinement and enhancement and can have larger wave vectors than light of the same frequency in vacuum. BSWs have been applied in nanoscale optical waveguides, sensing, fluorescence emission enhancement or sorting, surface-enhanced Raman scattering, and so on [3–12]. They can also realize the giant Goos-Hänchen shift, which will improve the functionality of sensors and may have an impact on the further development of sensor technology [13]. The BSWs are not subject to losses caused by absorption in metal, which allows for a BSW with a high resonance quality factor and a long propagation length. There are many choices of dielectric materials for BSWs, which allows this dielectric multilayer to be used from deep ultraviolet to near-infrared wavelengths [14]. SPPs can be sustained only in the transverse-magnetic (TM) polarization state [15–18], whereas BSWs can be either transverse-electric

(TE) or TM polarization. Previously, most work on BSWs related to the TE-polarized BSW [3–10,19], but not much work has been done on the TM-polarized one [11,12]. The reason is that the generation of TM-polarized BSWs is always affected by the Brewster angle effect [20]. There are no reports on energy coupling between the TE- and TM-polarized BSW or reports on how to transform the TE-polarized BSW into a TM-polarized one and vice versa. Polarization is one of the basic parameters for optical waves; hence, the ability to manipulate the polarization state of the electromagnetic surface waves can be of a fundamental importance for both science and technology. For example, it can increase the information capacity with a new parameter (polarization) involved in the surface waves, similar to the applications of cylindrical vector beams or orbital angular momentum in optical communications [21,22]. It can also introduce different light-matter interactions between electromagnetic surface waves and polarization-sensitive materials or cells. Although 3D waveguide-based polarization rotators are routinely used in modern photoelectric components and provide nearly unitary efficiency of polarization transformation [23,24], we have not seen any reports on the polarization rotators for 2D surface waves.

### II. THE DISPERSION RELATIONS OF THE BSW

The proposed dielectric multilayer that sustains both TE- and TM-polarized BSWs consists of 18 alternating dielectric layers of  $\text{Si}_3\text{N}_4$  and  $\text{SiO}_2$  as shown in Fig. 1(a).

\*dgzhang@ustc.edu.cn

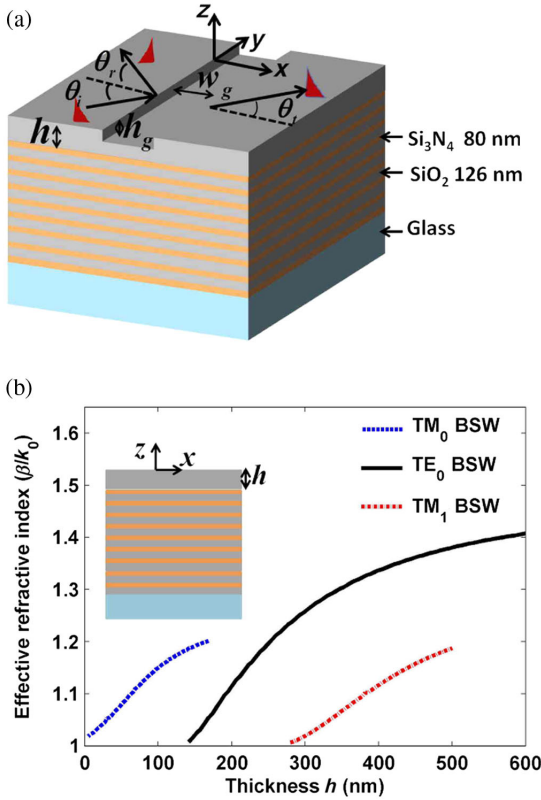


FIG. 1. (a) Schematic illustration of the dielectric multilayer. The dielectric multilayer consists of 18 alternating dielectric layers of  $\text{Si}_3\text{N}_4$  (80 nm thick) and  $\text{SiO}_2$  (126 nm thick). The thickness of the top  $\text{SiO}_2$  layer can be varied and is denoted as  $h$ . A groove with a rectangular cross section is inscribed on the top  $\text{SiO}_2$  layer. The width and depth of the groove are denoted as  $w_g$  and  $h_g$ , respectively. (b) The effective refractive indices of the TE BSW and TM BSW modes versus the thickness  $h$  of the top  $\text{SiO}_2$  layer.

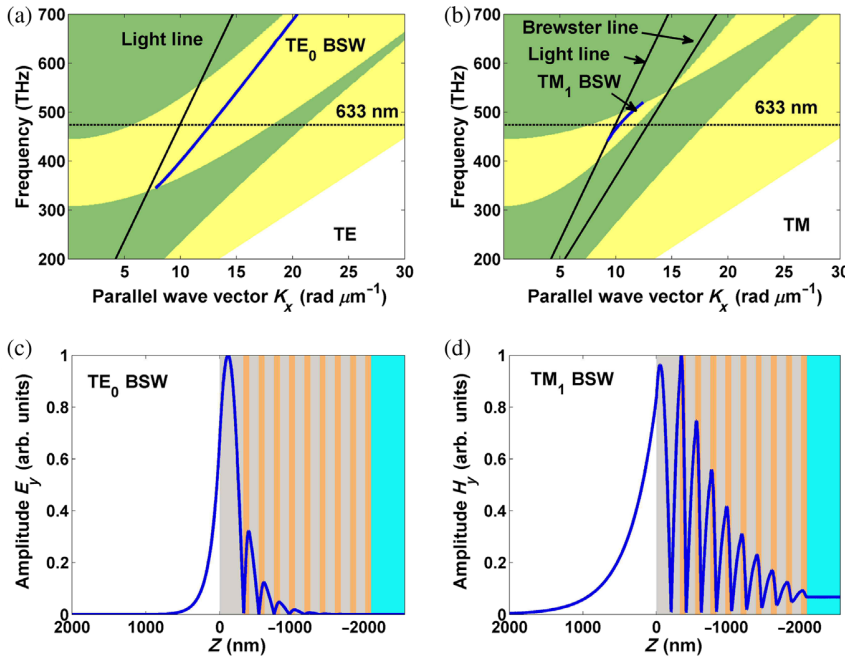
The refractive indices of the  $\text{Si}_3\text{N}_4$  and  $\text{SiO}_2$  layers are 2.65 and 1.48, respectively. The thicknesses of the  $\text{Si}_3\text{N}_4$  and  $\text{SiO}_2$  layers are fixed at 80 and 126 nm, respectively. The thickness of the top  $\text{SiO}_2$  layer can be varied and denoted as  $h$ . A rectangular groove with width  $w_g$  and depth  $h_g$  is inscribed on the top  $\text{SiO}_2$  layer. A BSW is obliquely incident on the groove. The symbols  $\theta_i$ ,  $\theta_r$ , and  $\theta_t$  denote the incidence, reflection, and transmission angles of the BSW, respectively. Different from the SPPs supported by the metal film, the dielectric multilayer can support the propagation of the TE BSW (the electric field perpendicular to the  $X$ - $Z$  plane) and the TM BSW (the magnetic field perpendicular to the  $X$ - $Z$  plane). Moreover, the propagation of the BSW is sensitive to the top layer's thickness  $h$  as shown in the inset of Fig. 1(b). Figure 1(b) demonstrates the change of the effective refractive indices of the TE BSW and TM BSW modes as a function of the top layer's thickness  $h$ . The effective refractive indices of the TE BSW and TM BSW modes decrease with the

decreasing thickness  $h$ . Compared with the case of the TE BSW modes, the TM BSW modes can be sustained by a dielectric multilayer in a very limited thickness range, which is attributed to the band-gap width of the dielectric multilayer for TM polarization being much smaller than that for TE polarization due to the Brewster effect of TM polarization. The photonic band gap of the dielectric multilayer and the dispersion relations for the TE BSW and TM BSW modes are shown in Figs. 2(a) and 2(b), respectively. The yellow zone denotes the photonic stop band of the dielectric multilayer. As the top layer's thickness is fixed at 320 nm, the dispersion curves for the  $\text{TE}_0\text{BSW}$  and  $\text{TM}_1\text{BSW}$  are also shown in Figs. 2(a) and 2(b), respectively. It is noted that the dispersion curve for the  $\text{TM}_1\text{BSW}$  can be held in a very limited frequency range due to the narrow band gap. To understand the waveguiding behaviors of the BSW, the field distributions for the  $\text{TE}_0\text{BSW}$  and  $\text{TM}_1\text{BSW}$  are shown in Figs. 2(c) and 2(d), respectively. A node of field for the  $\text{TM}_1\text{BSW}$  can be observed in the top layer, but there is no node in the top layer for the  $\text{TE}_0\text{BSW}$ . This is why the mode is named according to the number of field nodes in the top layer of the dielectric multilayer. In addition, the penetration depth of the  $\text{TM}_1\text{BSW}$  in the dielectric multilayer is larger than that of the  $\text{TE}_0\text{BSW}$  due to the narrow band gap. As noted in Fig. 1(b), the dielectric multilayer can sustain the  $\text{TE}_0\text{BSW}$  and  $\text{TM}_1\text{BSW}$  modes with thickness  $h$  ranging from 300 to 500 nm.

### III. POLARIZATION TRANSFORMATION OF THE BSW

#### A. The case of the single groove

Here, a groove is fabricated on the dielectric multilayer as shown in Fig. 1(a). As the BSW is obliquely incident on the groove, the interpolarization coupling between the TE BSW and TM BSW occurs due to the discontinuous interface in addition to the partial reflection and transmission of the BSW. The reflection, transmission, and polarization transformation intensities of the  $\text{TE}_0\text{BSW}$  and  $\text{TM}_1\text{BSW}$  as a function of the incidence angle are shown in Figs. 3(a) and 3(b), respectively. The results are obtained by the mode-matching method [25,26]. The validity of the mode-matching method is confirmed by comparing with the results obtained from the finite-difference frequency domain (FDFD) method [27]. The detailed descriptions of the simulation process are given in the Appendix. For the incident wave  $\text{TE}_0\text{BSW}$ ,  $R_{ss}$  and  $T_{ss}$  denote the reflection and transmission intensities of the  $\text{TE}_0\text{BSW}$ , and  $R_{sp}$  and  $T_{sp}$  denote the reflection and transmission intensities of the  $\text{TM}_1\text{BSW}$ , which are excited by the incident  $\text{TE}_0\text{BSW}$ . Similarly, for the incident wave  $\text{TM}_1\text{BSW}$ ,  $R_{pp}$  and  $T_{pp}$  denote the reflection and transmission intensities of the  $\text{TM}_1\text{BSW}$ , and  $R_{ps}$  and  $T_{ps}$  denote the reflection and transmission intensities of the  $\text{TE}_0\text{BSW}$  excited by the



$\text{TM}_1$  BSW. To facilitate the comparison of the polarization transformation efficiency of the BSW, the intensities  $R_{sp}$ ,  $R_{ps}$ ,  $T_{sp}$ , and  $T_{ps}$  are magnified by a factor of 10 in the curves shown in Figs. 3(a) and 3(b).

As the BSW propagates across the groove, the reflection and transmission of the BSW are well related to the difference of the effective refractive indices of the BSW inside and outside of the groove. Because the effective refractive index of the  $\text{TE}_0$  BSW is larger than that of the  $\text{TM}_1$  BSW for the same top layer's thickness, the reflection and transmission curves of the  $\text{TE}_0$  BSW demonstrate much more drastic changes at the large incidence angle. For example, as the incidence angle of the  $\text{TE}_0$  BSW is larger than  $50^\circ$ , the reflection intensity of the  $\text{TE}_0$  BSW is dramatically increased with the increasing incidence angle, and it finally approaches one as shown in Fig. 3(a). The polarization transformation  $R_{sp}$  from the  $\text{TE}_0$  BSW to the  $\text{TM}_1$  BSW is first increased with the increasing incidence angle, but it finally disappears around  $55^\circ$  due to the total internal reflection of the  $\text{TM}_1$  BSW, which is determined by matching the transverse wave vector,

$$k_0 n_{\text{eff},\text{BSW}}^{\text{TE}_0} \sin \theta_i = k_0 n_{\text{eff},\text{BSW}}^{\text{TM}_1} \sin \theta_r, \quad (1)$$

where  $n_{\text{eff},\text{BSW}}^{\text{TE}_0}$  and  $n_{\text{eff},\text{BSW}}^{\text{TM}_1}$  are the effective refractive indices of the  $\text{TE}_0$  BSW and  $\text{TM}_1$  BSW, respectively. Because the effective refractive index of the  $\text{TM}_1$  BSW is smaller than that of the  $\text{TE}_0$  BSW, the total internal reflection angle of the  $\text{TM}_1$  BSW is expressed as  $\theta_c^{\text{TM}_1} = \arcsin(n_{\text{eff},\text{BSW}}^{\text{TM}_1}/n_{\text{eff},\text{BSW}}^{\text{TE}_0})$ . In contrast, as the incident BSW is the  $\text{TM}_1$  BSW, the total internal reflection cannot occur, and the reflected angle of the  $\text{TE}_0$  BSW excited by the  $\text{TM}_1$  BSW can be expressed as

FIG. 2. The projected band structure of the dielectric multilayer for (a) TE polarization and (b) TM polarization. The yellow zone denotes the stop band. The blue solid lines denote the dispersion curves for the BSW with thickness  $h = 320$  nm. (c) The electric field distribution for the  $\text{TE}_0$  BSW. (d) The magnetic field distribution for the  $\text{TM}_1$  BSW. The field distributions are calculated at a wavelength of 633 nm.

$\theta_r^{\text{TE}_0} = \arcsin(n_{\text{eff},\text{BSW}}^{\text{TM}_1} \sin \theta_i / n_{\text{eff},\text{BSW}}^{\text{TE}_0})$ . There will be two reflected beams propagating along different directions due to the different effective refractive indices for the  $\text{TE}_0$  BSW and  $\text{TM}_1$  BSW at the same top layer's thickness, as the BSW is obliquely incident on the groove. In addition to the incidence angle, the depth and width of the groove can also affect the polarization transformation efficiency of the BSW. The influences of the depth and width of the groove on the polarization transformation efficiency of the  $\text{TE}_0$  BSW are shown in Fig. 4.

To evaluate the polarization transformation efficiency of the  $\text{TE}_0$  BSW, the scattering loss of the  $\text{TE}_0$  BSW is defined as

$$S_{\text{loss}} = 1 - R_{ss} - T_{ss} - R_{sp} - T_{sp}. \quad (2)$$

As the width of the groove is fixed at 400 nm, the polarization transformation intensity  $R_{sp}$  and the scattering loss  $S_{\text{loss}}$  of the  $\text{TE}_0$  BSW versus the depth of the groove and incidence angle are shown in Figs. 4(a) and 4(b), respectively. With the increasing depth of groove, the  $R_{sp}$  is increased, but the  $S_{\text{loss}}$  of the BSW is also increased. To balance the efficiency of polarization transformation and the scattering loss of the BSW, the depth of the groove is chosen to be 150 nm. In addition, the relationship of the polarization transformation intensity  $R_{sp}$  and the scattering loss  $S_{\text{loss}}$  of the BSW between the width of the groove and incidence angle are shown in Figs. 4(c) and 4(d), respectively. As the width of the groove is larger than 200 nm, the polarization transformation of the BSW becomes insensitive to the changes of the groove depth. Moreover, the scattering loss of the BSW will increase as the width of the groove is larger than 500 nm. Therefore, the depth and

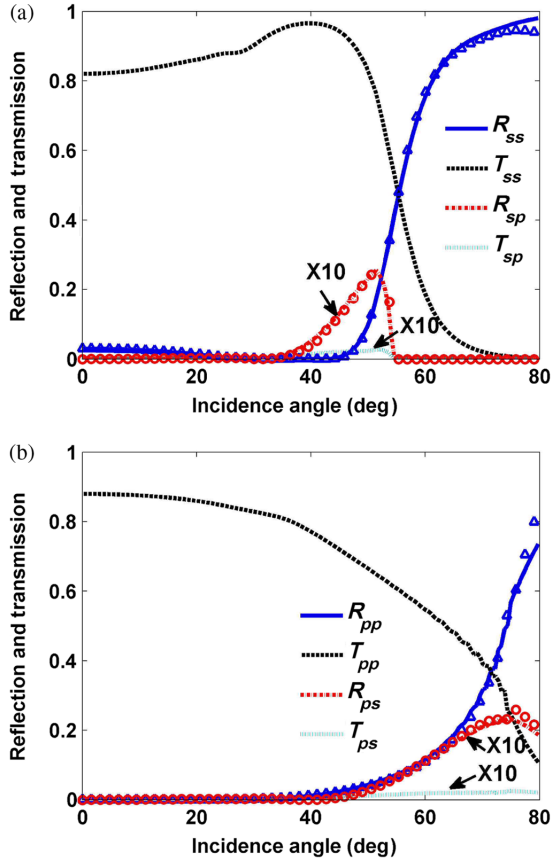


FIG. 3. (a) The reflection ( $R_{ss}$ ), transmission ( $T_{ss}$ ), and polarization transformation ( $R_{sp}$  and  $T_{sp}$ ) intensities of the  $TE_0$ BSW versus the angle of incidence. (b) The reflection ( $R_{pp}$ ), transmission ( $T_{pp}$ ), and polarization transformation ( $R_{ps}$  and  $T_{ps}$ ) intensities of the  $TM_1$ BSW versus the angle of incidence. The lines with triangles and circles denote the results obtained from the FDFD method. In simulation, the top layer's thickness  $h = 320$  nm, and the width  $w_g$  and depth  $h_g$  of the groove are 400 and 150 nm, respectively. The intensities of  $R_{sp}$ ,  $T_{sp}$ ,  $R_{ps}$ , and  $T_{ps}$  are magnified by a factor of 10. The incident wavelength of the light in vacuum is 633 nm.

width of the groove are chosen as 150 and 400 nm in the simulation to balance the efficiency of polarization transformation and the scattering loss of the BSW.

### B. The case of the two grooves

If multiple grooves are fabricated on the dielectric multilayer, this polarization transformation between the  $TE_0$ BSW and  $TM_1$ BSW can be enhanced or inhibited by the interference effect of multiple beams. As noted in Fig. 5, the two grooves are introduced into the structure, and the separation distance between the grooves is denoted as  $L_d$ . Figures 5(a) and 5(b) demonstrate the reflection, transmission, and polarization transformation intensities of the BSW as a function of the incidence angle. Compared to the case of the single groove, the reflection and

transmission intensities of the  $TE_0$ BSW exhibit a sharp dip and peak around an incidence angle of  $66^\circ$ , respectively. When the incidence angle of the  $TE_0$ BSW is larger than  $60^\circ$ , the single groove demonstrates the strong reflection of the  $TE_0$ BSW as shown in the Fig. 3(a). The groove is similar to a 2D partially reflecting mirror for the  $TE_0$ BSW. The two grooves with separation distance  $L_d$  can act as a 2D Fabry-Perot cavity, which contributes to the strong changes of reflection and transmission of the  $TE_0$ BSW. Furthermore, the polarization transformation intensity  $R_{sp}$  (from the  $TE_0$ BSW to  $TM_1$ BSW during reflection) is increased approximately fivefold compared to the case of the single groove as noted in Fig. 3(a). Similarly, the enhanced polarization transformation intensity  $R_{ps}$  (from the  $TM_1$ BSW to  $TE_0$ BSW during reflection) is also observed in Fig. 5(b).

## IV. DISCUSSION

### A. Generalized Fresnel formula for polarization transformation of the BSW

The enhanced polarization transformation of the BSW is attributed to the multiple reflections of the BSW in the two grooves. To describe the physical process of the polarization transformation of the BSW modes in the two grooves in detail, the Fresnel formula for the multilayer film is generalized to deal with the reflection and transmission of the BSW crossing the grooves. The groove can be considered as an equivalent interface. As the BSW propagates across the equivalent interface, the reflection, transmission, and polarization transformation of the BSW occur. A simplified model for multiple reflections of the BSW between the two grooves is demonstrated in the inset of Fig. 6. The structure is then divided into three parts by two equivalent interfaces. The three parts of the structure are numbered as 0, 1, and 2. The BSW is launched at the region 0. As the  $TE_0$ BSW propagates from region  $i$  to region  $j$ ,  $r_{ij}^{ss}$  and  $t_{ij}^{ss}$  denote the reflection and transmission coefficients, respectively, of the  $TE_0$ BSW.  $r_{ij}^{sp}$  and  $t_{ij}^{sp}$  denote the polarization transformation coefficients of the  $TE_0$ BSW to the  $TM_1$ BSW, respectively. Similarly, as the  $TM_1$ BSW transmits from region  $i$  to region  $j$ , the terms  $r_{ij}^{pp}$ ,  $t_{ij}^{pp}$ ,  $r_{ij}^{ps}$ , and  $t_{ij}^{ps}$  are used to denote the reflection, transmission, and polarization transformation coefficients, respectively, of the  $TM_1$ BSW. From the simplified model and the defined coefficients, the generalized Fresnel formula of the BSW can be expressed as

$$\begin{pmatrix} A_s^r \\ A_p^r \end{pmatrix} = (\tilde{\mathbf{R}} + \tilde{\mathbf{MST}}) \begin{pmatrix} A_s^i \\ A_p^i \end{pmatrix}, \quad (3)$$

where  $A_s^i$  and  $A_p^i$  denote the amplitude of the incident  $TE_0$ BSW and  $TM_1$ BSW, respectively.  $A_s^r$  and  $A_p^r$  denote the amplitude of the reflected  $TE_0$ BSW and  $TM_1$ BSW,

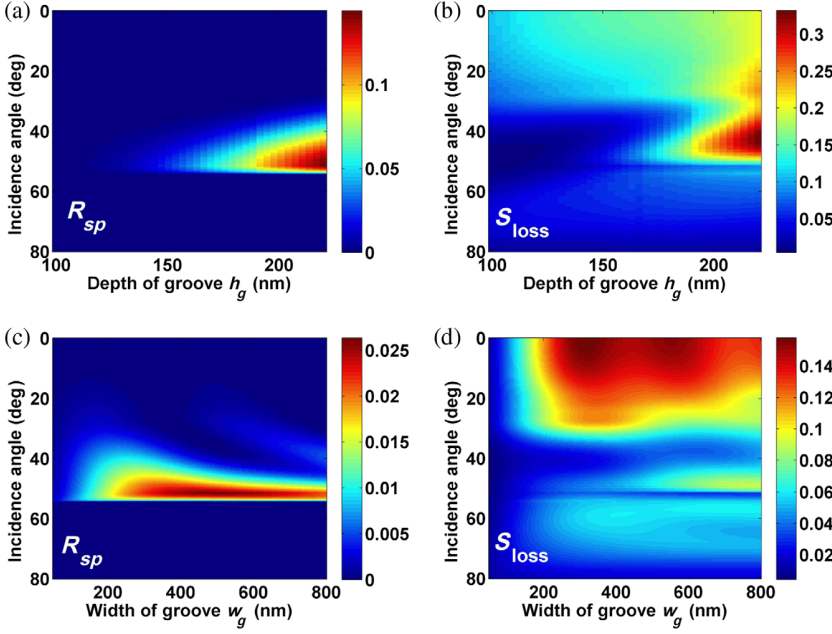


FIG. 4. The influences of the geometrical parameters of the groove on the polarization transformation of the BSW. (a) The polarization transformation intensity  $R_{sp}$  and (b) the scattering loss of the  $TE_0$ BSW as a function of the incidence angle and the depth of the groove. The width of the groove is fixed at 400 nm. As the depth of the groove is fixed at 150 nm, (c) shows the polarization transformation intensity  $R_{sp}$  and (d) shows the scattering loss of the  $TE_0$ BSW as a function of the incidence angle and the width of the groove.

respectively. As the BSW propagates across the two grooves, the reflection and polarization transformation coefficients of the BSW can be defined:

$$\begin{aligned} r_{012}^{ss} &= \left. \frac{A_s^r}{A_p^i} \right|_{A_p^i=0}, & r_{012}^{sp} &= \left. \frac{A_p^r}{A_s^i} \right|_{A_p^i=0}, \\ r_{012}^{ps} &= \left. \frac{A_s^r}{A_p^i} \right|_{A_s^i=0}, & r_{012}^{pp} &= \left. \frac{A_p^r}{A_p^i} \right|_{A_s^i=0}. \end{aligned} \quad (4)$$

In Eq. (3), the terms  $\tilde{\mathbf{R}}$  and  $\tilde{\mathbf{T}}$  denote the matrix of the reflection and transmission coefficients at the first groove, i.e., the first equivalent interface,

$$\tilde{\mathbf{R}} = \begin{pmatrix} r_{01}^{ss} & r_{01}^{ps} \\ r_{01}^{sp} & r_{01}^{pp} \end{pmatrix}, \quad \tilde{\mathbf{T}} = \begin{pmatrix} t_{01}^{ss} & t_{01}^{ps} \\ t_{01}^{sp} & t_{01}^{pp} \end{pmatrix}. \quad (5)$$

The matrix  $\mathbf{M}$  and  $\mathbf{S}$  describe the multiple reflections of the BSW between the two equivalent interfaces,

$$\mathbf{M} = \begin{pmatrix} t_{10}^{ss} r_{12}^{ss} e^{2i\gamma_s L_d} + t_{10}^{ps} r_{12}^{sp} e^{i(\gamma_s + \gamma_p)L_d}, & t_{10}^{ss} r_{12}^{ps} e^{i(\gamma_s + \gamma_p)L_d} + t_{10}^{ps} r_{12}^{pp} e^{2i\gamma_p L_d}, \\ t_{10}^{sp} r_{12}^{ss} e^{2i\gamma_s L_d} + t_{10}^{pp} r_{12}^{sp} e^{i(\gamma_s + \gamma_p)L_d}, & t_{10}^{sp} r_{12}^{ps} e^{i(\gamma_s + \gamma_p)L_d} + t_{10}^{pp} r_{12}^{pp} e^{2i\gamma_p L_d} \end{pmatrix}, \quad (6)$$

$$\mathbf{S} = \begin{pmatrix} 1 - r_{10}^{ss} r_{12}^{ss} e^{2i\gamma_s L_d} - r_{10}^{ps} r_{12}^{sp} e^{i(\gamma_s + \gamma_p)L_d}, & -r_{10}^{ss} r_{12}^{ps} e^{i(\gamma_s + \gamma_p)L_d} - r_{10}^{ps} r_{12}^{pp} e^{2i\gamma_p L_d}, \\ -r_{10}^{sp} r_{12}^{ss} e^{2i\gamma_s L_d} - r_{10}^{pp} r_{12}^{sp} e^{i(\gamma_s + \gamma_p)L_d}, & 1 - r_{10}^{sp} r_{12}^{ps} e^{i(\gamma_s + \gamma_p)L_d} - r_{10}^{pp} r_{12}^{pp} e^{2i\gamma_p L_d} \end{pmatrix}^{-1}. \quad (7)$$

Here, the terms  $\gamma_s = \sqrt{k_0^2(n_{\text{eff,BSW}}^{\text{TE}_0})^2 - k_y^2}$  and  $\gamma_p = \sqrt{k_0^2(n_{\text{eff,BSW}}^{\text{TM}_1})^2 - k_y^2}$  are the longitudinal wave numbers of the  $TE_0$ BSW and  $TM_1$ BSW, respectively, along the  $X$  axis.  $k_y$  is the transverse wave number of the BSW along the  $Y$  axis. Then, the reflection intensities  $R_{ss}$  and  $R_{pp}$  can be expressed as

$$R_{ss} = |r_{012}^{ss}|^2, \quad R_{pp} = |r_{012}^{pp}|^2. \quad (8)$$

The polarization transformation intensities  $R_{sp}$  and  $R_{ps}$  are given by

$$R_{sp} = |r_{012}^{sp}|^2 \frac{P_{x,r}^{\text{TM}_1}}{P_{x,\text{in}}^{\text{TE}_0}}, \quad R_{ps} = |r_{012}^{ps}|^2 \frac{P_{x,r}^{\text{TE}_0}}{P_{x,\text{in}}^{\text{TM}_1}}. \quad (9)$$

The terms  $P_{x,r}^*$  and  $P_{x,in}^*$  denote the propagation power along the  $X$  axis for the reflected and incident BSW modes, respectively.

Figure 6(a) demonstrates the polarization transformation coefficient  $r_{012}^{sp}$  for the  $TE_0$ BSW propagating across two grooves versus the incidence angle. The solid line denotes the results obtained from the generalized Fresnel

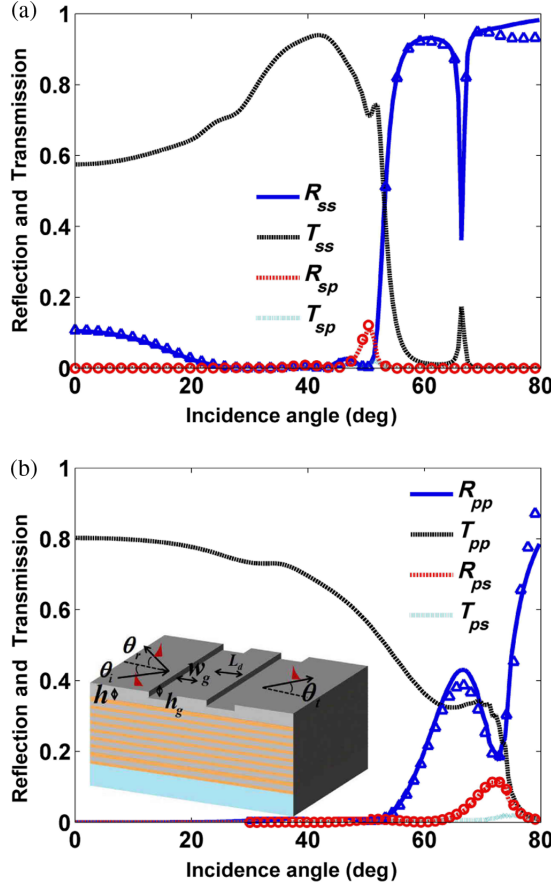


FIG. 5. Reflection, transmission, and polarization transformation intensities versus the incidence angle for (a) the incident wave TE<sub>0</sub>BSW and (b) the incident wave TM<sub>1</sub>BSW. The lines with triangles and circles denote the results obtained from the FDFD method. Here, two grooves with separation distance  $L_d$  are inscribed in the top SiO<sub>2</sub> layer. The wavelength is 633 nm. The thickness of the top layer is 320 nm. The width  $w_g$  and the depth  $h_g$  of the groove are 400 and 150 nm, respectively. The separation distance  $L_d$  between the grooves is 400 nm.

formula shown in Eq. (4), and the triangles denote the results obtained from the mode-matching method. To facilitate the comparison of the polarization transformation enhanced by two grooves, the transformation coefficient  $r^{sp}$  of the TE<sub>0</sub>BSW for a single groove is also shown in the Fig. 6(a) with a dotted line. It is noted that the transformation coefficient  $r_{012}^{sp}$  of the TE<sub>0</sub>BSW can be enhanced or inhibited at the certain incidence angle relative to the coefficient  $r^{sp}$ , which is attributed to the interference effect between the multiple beams. Similarly, the polarization transformation coefficient  $r_{012}^{ps}$  for the TM<sub>1</sub>BSW propagating across two grooves versus the incidence angle is shown in Fig. 6(b). Compared to the transformation coefficient  $r^{ps}$  for a single groove, the coefficient  $r_{012}^{ps}$  can also be enhanced or inhibited at a certain incidence angle due to the interference effect from

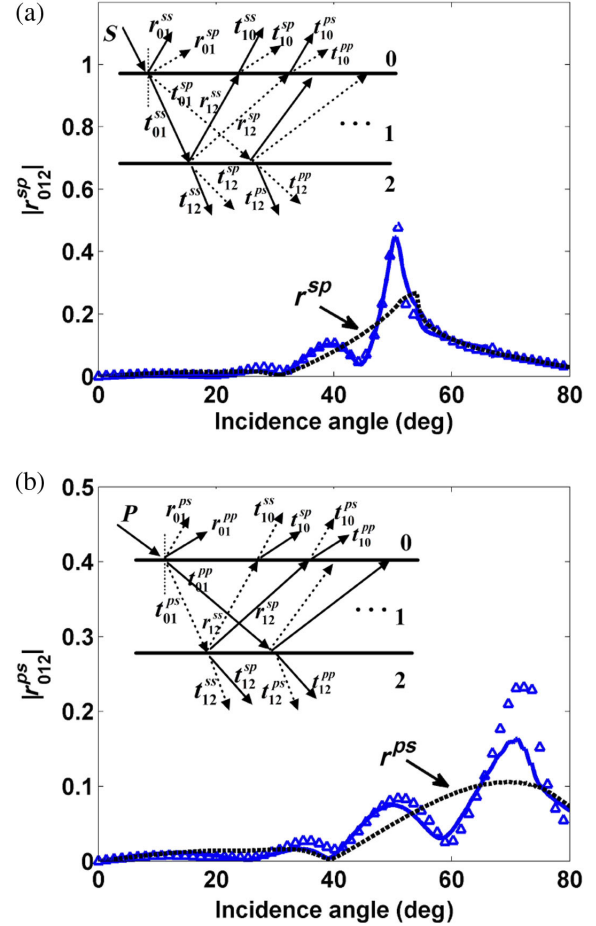


FIG. 6. The amplitude of the polarization transformation coefficients as a function of the incidence angle (a)  $r_{012}^{sp}$  for the polarization transformation of the TE<sub>0</sub>BSW to the TM<sub>1</sub>BSW, (b)  $r_{012}^{ps}$  for the polarization transformation of the TM<sub>1</sub>BSW to the TE<sub>0</sub>BSW. The solid lines denote the results obtained from Eq. (4), and the triangles denote the results obtained from the mode-matching method. The black dotted line denotes the polarization transformation coefficient of the BSW for a single groove. The insets in the figure describe the simplified model of multiple reflection of the BSW between the two grooves.

the reflected beams. The interference effects are sensitive to the phase factors of the reflected beam, which are well related to the wave number  $\gamma_s$ ,  $\gamma_p$ , and the separation distance  $L_d$  noted in Eqs. (6) and (7). Then, this guidance is a practical way to control the polarization transformation of the BSW by adjusting the separation distance  $L_d$  between the grooves.

## B. Anomalous reflection of the BSW

As the TE<sub>0</sub>BSW propagates across the two grooves, Figs. 7(a) and 7(b) demonstrate the polarization transformation intensity  $R_{sp}$  and the reflection intensity  $R_{ss}$  as a function of the incidence angle and the separation distance  $L_d$ , respectively. With increasing the separation

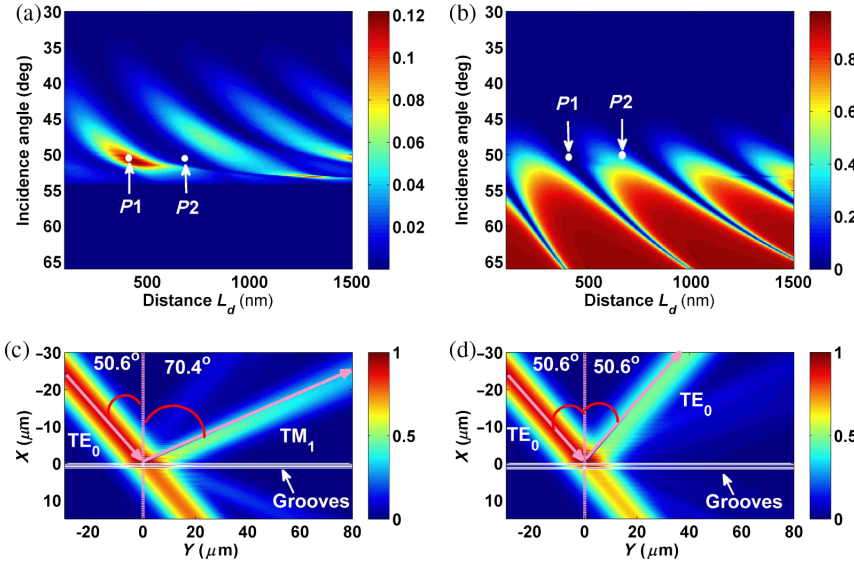


FIG. 7. (a) Polarization transformation intensity  $R_{sp}$  and (b) the reflection intensity  $R_{ss}$  of the TE<sub>0</sub>BSW versus the incidence angle and the separation distance  $L_d$  between the grooves. The incidence angle of the TE<sub>0</sub>BSW is fixed at 50.6°. The electric field intensity distributions for different separation distances (c)  $L_d = 410$  nm and (d)  $L_d = 680$  nm. The wavelength of the incident light in vacuum is 633 nm.

distance  $L_d$ ,  $R_{sp}$  and  $R_{ss}$  exhibit periodic changes arising from the constructive and destructive interference of the reflected BSW beams. Furthermore, the changes of  $R_{sp}$  and  $R_{ss}$  demonstrate the different periodicity due to the different interference effect noted in Eqs. (6) and (7). It is feasible to achieve a complete polarization transformation in the reflected beam by adjusting the distance  $L_d$ , such as the point  $P1$  labeled in Figs. 7(a) and 7(b). The point  $P1$  means that the incidence angle of the TE<sub>0</sub>BSW is 50.6°, and the separation distance  $L_d$  is 410 nm.  $R_{sp}$  can achieve the maximum value, and the value of  $R_{ss}$  can become the minimum value at this condition denoted by point  $P1$ . The electric field distribution of the structure is calculated by the mode-matching method at this condition, as shown in Fig. 7(c). The electric fields are extracted at the location  $z = 10$  nm ( $X$ - $Y$  plane). The incident TE<sub>0</sub>BSW beam is modeled as the Gaussian shape with half-width  $10\lambda$ , and  $\lambda = 633$  nm is the incident wavelength. An interesting phenomenon is observed in Fig. 7(c). The reflection angle of the beam relative to the normal direction of the grooves is larger than the incident angle due to the excitation of the TM<sub>1</sub>BSW. The reflection angle of the beam can be predicted from Eq. (1) and is equal to 70.4°. This anomalous reflection is attributed to the polarization transformation of the BSW, which is different from that arising from a metasurface or metagratings [28–31]. Then, the grooves can be used as the mode converter or polarization rotator for the BSWs.

In addition, the generation of the TM<sub>1</sub>BSW can also be inhibited by changing the distance  $L_d$ . For example, as the distance  $L_d$  is increased to 680 nm, the value of  $R_{sp}$  becomes minimal due to the destructive interference of the beams, but the value of  $R_{ss}$  is increased corresponding to the point  $P2$  in Figs. 7(a) and 7(b). At this condition, the

total electric field distribution is calculated and shown in Fig. 7(d). In this case, the structure demonstrates the normal reflection. The reflection angle of the beam is equal to the incident angle. The polarization of the reflection beam is the same as that of the incident beam. Therefore, the separation distance  $L_d$  between the grooves is an efficient parameter to control the polarization transformation of the BSW.

### C. The effect of the multiple grooves

It is noted that most of the energy of the TE<sub>0</sub>BSW can also transmit across the grooves as shown in Fig. 7(c). This part of the energy can be further transformed to that of the TM<sub>1</sub>BSW by increasing the reflection of TE<sub>0</sub>BSW, which can be achieved by increasing the number of grooves. Figure 8(a) demonstrates the polarization transformation intensity  $R_{sp}$  versus the incidence angle with different numbers of grooves. The separation distance  $L_d$  between the grooves is fixed at 400 nm. It is noted that the peak value of the polarization transformation intensity  $R_{sp}$  around 50.6° is enhanced by increasing the number of grooves. As the distance  $L_d$  is increased to 680 nm, the constructive interference condition of polarization transformation  $R_{sp}$  is changed to 45.8°. By increasing the number of grooves, the peak value of polarization transformation intensity  $R_{sp}$  around 45.8° is also enhanced, which is shown in Fig. 8(b). To evaluate the maximum value of  $R_{sp}$  achieved by the multiple grooves, the peak values of  $R_{sp}$  at the different distance  $L_d$  versus the number of grooves are shown in Fig. 8(c). It is noted the values of  $R_{sp}$  can approach the stable values as the number of grooves  $N_g$  is greater than 10. The maximum polarization transformation efficiency of the TE<sub>0</sub>BSW to TM<sub>1</sub>BSW achieved by the multiple grooves can approach 43%.

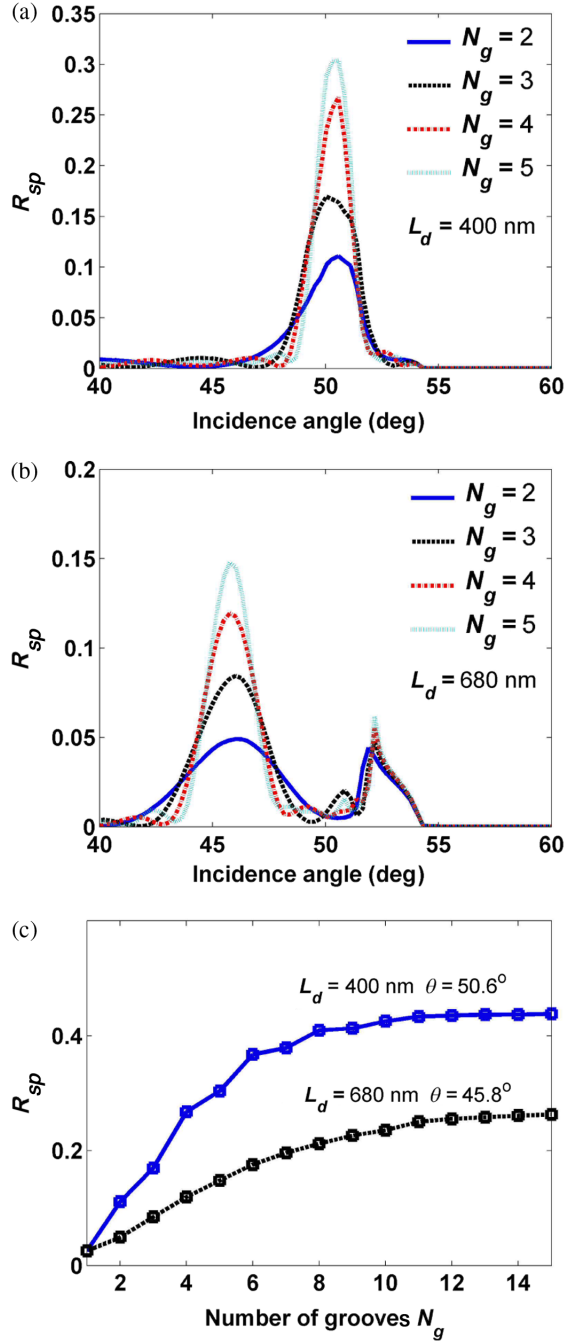


FIG. 8. Polarization transformation intensity  $R_{sp}$  as a function of the incidence angle with different numbers of grooves. The separation distance  $L_d$  between the grooves is (a) 400 and (b) 680 nm. (c) The maximum transformation intensity  $R_{sp}$  versus the number of grooves  $N_g$  at different separation distance  $L_d$ .

## V. CONCLUSION

In conclusion, the polarization transformation between the TE- and TM-polarized BSW is achieved through the multiple reflections from the grooves inscribed on a dielectric multilayer. By tuning the depth of the groove and the

separation distance between grooves, a polarization transformation efficiency can be reached as high as 43% attributed to the constructive interference of the reflected beams. This value is much larger than the case of surface waves to free-space waves [32], where the transformation efficiency is only 0.4%. In addition, to the best of our knowledge, we are not aware of reports on the polarization transformation of any surface waves. Because of this polarization transformation between the two polarized BSWs, an anomalous reflection phenomenon appears in which the reflection angle of the beam is different from the incidence angle. This phenomenon is different from the anomalous reflection induced by the widely investigated metasurfaces and provides a means to manipulate the polarization and reflection of the electromagnetic waves [28–31]. Furthermore, the polarization transformation of the BSW can be adjusted by changing the separation distance between the grooves. This provides a feasible way to strengthen or inhibit the polarization transformation of the BSW in an on-chip optical circuit system. The proposed method for polarization transformation can be used not only in the dielectric multilayer for BSWs, but it is also applicable to the planar waveguide containing two waveguide modes of different polarization states [33]. Our work has potential applications in various areas, such as lab-on-a-chip devices, biosensing, and imaging, among others. We have already reported that the different penetration depths above the surface can be used for selective sensing from the surface and bulk volume regions of the samples [33].

## ACKNOWLEDGMENTS

This work was supported by Ministry of Science and Technology of the People's Republic of China (2013CBA01703 and 2016YFA0200601), National Natural Science Foundation of China (61427818, 11774330 and 11374286), the Science and Technological Fund of Anhui Province for Outstanding Youth (1608085J02), the Fundamental Research Funds for the Central Universities (WK2030380008), and the Longshan academic talent research supporting program of Southwest University of Science and Technology (17LZX626). This work was also supported by grants from the National Institute of Health (GM107986, EB006521, EB018959, and OD019975).

## APPENDIX: FDFD SIMULATIONS OF THE PROPOSED DIELECTRIC MULTILAYER

The structure's translation invariance is along the  $Y$  axis. As the BSW is obliquely incident on the groove with the incidence angle  $\theta_i$ , the field components of the BSW can be written as

$$\psi(x, y, z) = \varphi(x, z) e^{i\beta \sin \theta_i y}, \quad (\text{A1})$$

where  $\beta$  is the transverse wave number of the BSW. By normalizing the magnetic field  $\vec{\tilde{H}} = i\sqrt{\mu_0/\epsilon_0}\vec{H}$ , the Maxwell equations can be written as

$$\nabla \times \vec{E} = k_0 \mu_r \vec{\tilde{H}}, \quad \nabla \times \vec{\tilde{H}} = k_0 \epsilon \vec{E}. \quad (\text{A2})$$

It is reasonable to assume the relative permeability  $\mu_r = 1$  for the normal dielectric. According to the form of field components in Eq. (A1), the Maxwell equations can be expressed as

$$\begin{aligned} \tilde{H}_x &= \frac{k_0^2 \epsilon}{k_0^2 \epsilon - \beta^2 \sin^2 \theta_i} \left[ \frac{i\beta \sin \theta_i}{k_0^2 \epsilon} \frac{\partial \tilde{H}_y}{\partial x} - \frac{1}{k_0} \frac{\partial E_y}{\partial z} \right], \\ E_x &= \frac{k_0^2 \epsilon}{k_0^2 \epsilon - \beta^2 \sin^2 \theta_i} \left[ \frac{i\beta \sin \theta_i}{k_0^2 \epsilon} \frac{\partial E_y}{\partial x} - \frac{1}{k_0 \epsilon} \frac{\partial \tilde{H}_y}{\partial z} \right], \\ \tilde{H}_z &= \frac{k_0^2 \epsilon}{k_0^2 \epsilon - \beta^2 \sin^2 \theta_i} \left[ \frac{1}{k_0} \frac{\partial E_y}{\partial x} + \frac{i\beta \sin \theta_i}{k_0^2 \epsilon} \frac{\partial \tilde{H}_y}{\partial z} \right], \\ E_z &= \frac{k_0^2 \epsilon}{k_0^2 \epsilon - \beta^2 \sin^2 \theta_i} \left[ \frac{1}{k_0 \epsilon} \frac{\partial \tilde{H}_y}{\partial x} + \frac{i\beta \sin \theta_i}{k_0^2 \epsilon} \frac{\partial E_y}{\partial z} \right], \end{aligned} \quad (\text{A3})$$

$$\begin{aligned} \frac{\partial E_x}{\partial z} - \frac{\partial E_z}{\partial x} &= k_0 \tilde{H}_y, \\ \frac{\partial \tilde{H}_x}{\partial z} - \frac{\partial \tilde{H}_z}{\partial x} &= k_0 \epsilon E_y. \end{aligned} \quad (\text{A4})$$

By substituting Eq. (A3) into Eq. (A4), a coupled equation can be obtained,

$$\begin{aligned} M_{pp} \tilde{H}_y + M_{ps} E_y &= 0, \\ M_{sp} \tilde{H}_y + M_{ss} E_y &= 0, \end{aligned} \quad (\text{A5})$$

$$\begin{aligned} M_{pp} &= - \left[ \frac{\partial}{\partial z} \left( \kappa \frac{\partial}{\partial z} \right) + \frac{\partial}{\partial x} \left( \kappa \frac{\partial}{\partial x} \right) + k_0^2 \right], \\ M_{ps} = M_{sp} &= \frac{i\beta \sin \theta_i}{k_0} \left[ \frac{\partial}{\partial z} \left( \kappa \frac{\partial}{\partial x} \right) - \frac{\partial}{\partial x} \left( \kappa \frac{\partial}{\partial z} \right) \right], \\ M_{ss} &= - \left[ \frac{\partial}{\partial z} \left( \kappa \epsilon \frac{\partial}{\partial z} \right) + \frac{\partial}{\partial x} \left( \kappa \epsilon \frac{\partial}{\partial x} \right) + k_0^2 \epsilon \right], \end{aligned} \quad (\text{A6})$$

where  $\kappa = k_0^2 / (k_0^2 \epsilon - \beta^2 \sin^2 \theta)$ ,  $k_0$  is the wave number of light in vacuum, and  $\epsilon$  is the dielectric function distribution of the structure in the  $X$ - $Z$  plane. Equations (A5) and (A6) can be solved by using the FDFD method. In the FDFD method, Eqs. (A5) and (A6) are discretized using Yee's mesh, which can be further written in a matrix format:

$$\begin{aligned} \tilde{M}_{pp} \tilde{H}_y + \tilde{M}_{ps} E_y &= 0, \\ \tilde{M}_{sp} \tilde{H}_y + \tilde{M}_{ss} E_y &= 0, \end{aligned} \quad (\text{A7})$$

$$\begin{aligned} \tilde{M}_{pp} &= -[\mathbf{D}_z^E \boldsymbol{\kappa} \mathbf{D}_z^H + \mathbf{D}_x^E \boldsymbol{\kappa} \mathbf{D}_x^H + k_0^2 \mathbf{I}], \\ \tilde{M}_{ps} &= \frac{i\beta \sin \theta_i}{k_0} [\mathbf{D}_z^E \boldsymbol{\kappa} \mathbf{D}_x^E - \mathbf{D}_x^E \boldsymbol{\kappa} \mathbf{D}_z^E], \\ \tilde{M}_{sp} &= \frac{i\beta \sin \theta_i}{k_0} [\mathbf{D}_z^H \boldsymbol{\kappa} \mathbf{D}_x^H - \mathbf{D}_x^H \boldsymbol{\kappa} \mathbf{D}_z^H], \\ \tilde{M}_{ss} &= -[\mathbf{D}_z^H \boldsymbol{\kappa} \mathbf{D}_z^E + \mathbf{D}_x^H \boldsymbol{\alpha} \boldsymbol{\epsilon} \mathbf{D}_x^E + k_0^2 \boldsymbol{\epsilon}]. \end{aligned} \quad (\text{A8})$$

Here, the terms  $\mathbf{D}_x^E$ ,  $\mathbf{D}_z^E$ ,  $\mathbf{D}_x^H$ , and  $\mathbf{D}_z^H$  are band matrices determined by the first-order spatial derivatives of the electric fields and magnetic fields, respectively. In Eqs. (A7) and (A8),  $\tilde{M}_{pp}$  and  $\tilde{M}_{ss}$  are the generated matrices for the TM BSW and TE BSW, respectively.  $\tilde{M}_{ps}$  and  $\tilde{M}_{sp}$  are the polarization transformation matrices between the TE BSW and TM BSW, which are well related to the incidence angle of the BSW and the distribution of the dielectric function. As the BSW is normally incident on the groove, the TE BSW and TM BSW will be decoupled. In addition, Eq. (A7) also demonstrates the different electromagnetic behaviors between the BSW and homogeneous plane wave. The homogeneous plane wave is generally considered to be invariant along the  $Z$  direction (that is, the direction of the wave front), i.e.,  $\mathbf{D}_z^E = 0$  and  $\mathbf{D}_z^H = 0$ . Then, Eq. (A7) is also decoupled. Therefore, the TE- and TM-polarized plane waves cannot be coupled as the plane wave is obliquely incident on the laterally continuous structure.

To simulate the propagation of the BSW, it can be introduced into Eq. (A7) by the total-field–scattering-field technique. The perfectly matched layers absorbing the boundary conditions are utilized around the structure to avoid reflection of the electromagnetic wave at the boundary. Then, the electromagnetic responses of the structure can be obtained by solving Eq. (A7). The reflection and polarization transformation coefficients of the BSW can be found by projecting the simulated fields extracted on the received plane onto the BSW mode profile. According to the orthogonal relation of the eigenmode, the total field can be projected onto any eigenmode,

$$E_{z,\text{total}} = \sum_k A_k e_{z,k}, \quad \tilde{H}_{z,\text{total}} = \sum_k B_k \tilde{h}_{z,k}, \quad (\text{A9})$$

where the  $e_{z,k}$  and  $\tilde{h}_{z,k}$  are field components along the  $Z$  axis for the  $k$ th eigenmode. Then, as the incident BSW is TE polarized, the coefficients  $r^{ss}$  ad  $r^{sp}$  can be obtained as

$$r^{ss} = \frac{\int e_{y,\text{BSW}} \tilde{H}_{z,\text{total}} dz}{\int e_{y,\text{BSW}} \tilde{h}_{z,\text{BSW}} dz}, \quad r^{sp} = \frac{\int \tilde{h}_{y,\text{BSW}} E_{z,\text{total}} dz}{\int \tilde{h}_{y,\text{BSW}} e_{z,\text{BSW}} dz}. \quad (\text{A10})$$

Similarly, as the incident BSW is TM polarized, the coefficients  $r^{pp}$  and  $r^{ps}$  can also be found:

$$r^{pp} = \frac{\int \tilde{h}_{y,\text{BSW}} E_{z,\text{total}} dz}{\int \tilde{h}_{y,\text{BSW}} e_{z,\text{BSW}} dz}, \quad r^{ps} = \frac{\int e_{y,\text{BSW}} \tilde{H}_{z,\text{total}} dz}{\int e_{y,\text{BSW}} \tilde{h}_{z,\text{BSW}} dz}. \quad (\text{A11})$$

- [1] R. D. Meade, K. D. Brommer, A. M. Rappe, and J. D. Joannopoulos, Electromagnetic Bloch waves at the surface of a photonic crystal, *Phys. Rev. B* **44**, 10961(R) (1991).
- [2] P. Yeh, A. Yariv, and C. S. Hong, Electromagnetic propagation in periodic stratified media. I. General theory, *J. Opt. Soc. Am.* **67**, 423 (1977).
- [3] A. Sinibaldi, N. Danz, E. Descrovi, P. Munzert, U. Schulz, F. Sonntag, L. Dominici, and F. Michelotti, Direct comparison of the performance of Bloch surface wave and surface plasmon polariton sensors, *Sens. Actuators B* **174**, 292 (2012).
- [4] R. Badugu, K. Nowaczyk, E. Descrovi, and J. R. Lakowicz, Radiative decay engineering 6: Fluorescence on one-dimensional photonic crystals, *Anal. Biochem.* **442**, 83 (2013).
- [5] K. Toma, E. Descrovi, M. Toma, M. Ballarini, P. Mandracchi, F. Giorgis, A. Mateescu, U. Jonas, W. Knoll, and J. Dostalek, Bloch-surface wave-enhanced fluorescence biosensor, *Biosens. Bioelectron.* **43**, 108 (2013).
- [6] S. Pirotta, X. G. Xu, A. Delfan, S. Mysore, S. Maiti, G. Dacarro, M. Patrini, M. Galli, G. Gutzett, D. Bajoni, J. E. Sipe, G. C. Walker, and M. Liscidini, Surface-enhanced Raman scattering in purely dielectric structures via Bloch surface waves, *J. Phys. Chem. C* **117**, 6821 (2013).
- [7] E. Descrovi, T. Sfez, M. Quaglio, D. Brunazzo, L. Dominici, F. Michelotti, H. P. Herzig, O. J. F. Martin, and F. Giorgis, Guided Bloch surface waves on ultrathin polymeric ridges, *Nano Lett.* **10**, 2087 (2010).
- [8] A. Angelini, A. Lamberti, S. Ricciardi, F. Frascella, P. Munzert, N. De Leo, and E. Descrovi, In-plane 2D focusing of surface waves by ultrathin refractive structures, *Opt. Lett.* **39**, 6391 (2014).
- [9] A. Angelini, E. Barakat, P. Munzert, L. Boarino, N. De Leo, E. Enrico, F. Giorgis, H. P. Herzig, C. F. Pirri, and E. Descrovi, Focusing and extraction of light mediated by Bloch surface waves, *Sci. Rep.* **4**, 5428 (2014).
- [10] A. Angelini, P. Munzert, E. Enrico, N. De Leo, L. Scaltrito, L. Boarino, F. Giorgis, and E. Descrovi, Surface-wave-assisted beaming of light radiation from localized sources, *ACS Photonics* **1**, 612 (2014).
- [11] A. Sinibaldi, A. Fieramosca, R. Rizzo, A. Anopchenko, N. Danz, P. Munzert, C. Magistris, C. Barolo, and F. Michelotti, Combining label-free and fluorescence operation of Bloch surface wave optical sensors, *Opt. Lett.* **39**, 2947 (2014).
- [12] J. Gao, A. M. Sarangan, and Q. Zhan, Polarization multiplexed fluorescence enhancer using a pixelated one-dimensional photonic band gap structure, *Opt. Lett.* **37**, 2640 (2012).
- [13] V. Soboleva, V. V. Moskalenko, and A. A. Fedyanin, Giant Goos-Hänchen Effect and Fano Resonance at Photonic Crystal Surfaces, *Phys. Rev. Lett.* **108**, 123901 (2012).
- [14] R. Badugu, J. Y. Mao, S. Blair, D. G. Zhang, E. Descrovi, A. Angelini, Y. P. Huo, and J. R. Lakowicz, Bloch surface wave-coupled emission at ultraviolet wavelengths, *J. Phys. Chem. C* **120**, 28727 (2016).
- [15] S. A. Maier, *Plasmonics: Fundamentals and Applications* (Springer New York, 2007).
- [16] H. Raether, *Surface Plasmons on Smooth and Rough Surfaces and on Gratings* (Springer-Verlag Berlin, 1988).
- [17] J. Lin, J. Dellinger, P. Genevet, B. Cluzel, F. de Fornel, and F. Capasso, Cosine-Gauss Plasmon Beam: A Localized Long-Range Nondiffracting Surface Wave, *Phys. Rev. Lett.* **109**, 093904 (2012).
- [18] P. Bharadwaj, A. Bouhelier, and L. Novotny, Electrical Excitation of Surface Plasmons, *Phys. Rev. Lett.* **106**, 226802 (2011).
- [19] L. Yu, E. Barakat, T. Sfez, L. Hvozdara, J. Di Francesco, and H. P. Herzig, Manipulating Bloch surface waves in 2D: A platform concept-based flat lens, *Light Sci. Appl.* **3**, e124 (2014).
- [20] M. Born and E. Wolf, *Principles of Optics*, 7th ed. (Cambridge University Press, Cambridge, England, 1999).
- [21] Q. W. Zhan, Cylindrical vector beams: From mathematical concepts to applications, *Adv. Opt. Photonics* **1**, 1 (2009).
- [22] A. M. Yao and M. J. Padgett, Orbital angular momentum: Origins, behavior and applications, *Adv. Opt. Photonics* **3**, 161 (2011).
- [23] R. C. Alferness and L. L. Buhl, Waveguide electro-optic polarization transformer, *Appl. Phys. Lett.* **38**, 655 (1981).
- [24] H. Heidrich, P. Albrecht, M. Hamacher, H. P. Nolting, H. Schroeter-Janssen, and C. M. Weinert, Passive mode converter with a periodically tilted InP/GaInAsP rib waveguide, *IEEE Photonics Technol. Lett.* **4**, 34 (1992).
- [25] H. Derudder, F. Olyslager, D. De Zutter, and S. Van den Berghe, Efficient mode-matching analysis of discontinuities in finite planar substrates using perfectly matched layers, *IEEE Trans. Antennas Propag.* **49**, 185 (2001).
- [26] P. Bienstman, Ph.D. thesis, Ghent University, 2001.
- [27] R. C. Rumpf, Ph.D. thesis, University of Central Florida, 2006.
- [28] N. F. Yu and F. Capasso, Flat optics with designer metasurfaces, *Nat. Mater.* **13**, 139 (2014).
- [29] A. V. Kildishev, A. Boltasseva, and V. M. Shalaev, Planar photonics with metasurfaces, *Science* **339**, 1232009 (2013).
- [30] N. Yu, P. Genevet, M. A. Kats, F. Aieta, J. P. Tetienne, F. Capasso, and Z. Gaburro, Light propagation with phase discontinuities: Generalized laws of reflection and refraction, *Science* **334**, 333 (2011).
- [31] Y. Ra'di, D. L. Sounas, and A. Alù, Metagratings: Beyond the Limits of Graded Metasurfaces for Wave Front Control, *Phys. Rev. Lett.* **119**, 067404 (2017).
- [32] G. I. Stegeman, N. E. Glass, A. A. Maradudin, T. P. Shen, and R. F. Wallis, Fresnel relations for surface polaritons at interfaces, *Opt. Lett.* **8**, 626 (1983).
- [33] R. Wang, D. Zhang, L. Zhu, X. Wen, J. Chen, C. Kuang, X. Liu, P. Wang, H. Ming, R. Badugu, and J. R. Lakowicz, Selectable surface and bulk fluorescence imaging with plasmon-coupled waveguides, *J. Phys. Chem. C* **119**, 22131 (2015).